How to cite: *Angew. Chem. Int. Ed.* **2023,** *62,* e202303480
doi.org/10.1002/anie.202303480

VIP **Ammonium-Ion Batteries** *Very Important Paper*

Reversible Ammonium Ion Intercalation/de-intercalation with Crystal Water Promotion Effect in Layered $VOPO_4{\cdot}2H_2O$**

*Fei Ye[+], Ruilvjing Pang[+], Chengjie Lu, Qiang Liu, Yuping Wu, Renzhi Ma, and Linfeng Hu**

Abstract: The non-metal NH_4^+ carrier has attracted tremendous interests for aqueous energy storage owing to its light molar mass and fast diffusion in aqueous electrolytes. Previous study inferred that NH_4^+ ion storage in layered $VOPO_4{\cdot}2H_2O$ is impossible due to the removal of NH_4^+ from NH_4VOPO_4 leads to a phase change inevitably. Herein, we update this cognition and demonstrated highly reversible intercalation/de-intercalation behavior of NH_4^+ in layered $VOPO_4{\cdot}2H_2O$ host. Satisfactory specific capacity of 154.6 $mAh\,g^{-1}$ at 0.1 $A\,g^{-1}$ and very stable discharge potential plateau at 0.4 V based on reference electrode was achieved in $VOPO_4{\cdot}2H_2O$. A rocking-chair ammonium-ion full cell with the $VOPO_4{\cdot}2H_2O$//2.0 M NH_4OTf//PTCDI configuration exhibited a specific capacity of 55 $mAh\,g^{-1}$, an average operating voltage of about 1.0 V and excellent long-term cycling stability over 500 cycles with a coulombic efficiency of ≈99 %. Theoretical DFT calculations suggest a unique crystal water substitution process by ammonium ion during the intercalation process. Our results provide new insight into the intercalation/de-intercalation of NH_4^+ ions in layered hydrated phosphates through crystal water enhancement effect.

Introduction

Sustainable rechargeable batteries have triggered tremendous demands in large-scale, cost-efficient and high-energy-density stationary energy storage systems.[1] The most recent progress on energy storage demonstrates that nonmetallic cations, e.g., proton (H^+), hydronium (H_3O^+), and ammonium (NH_4^+) ions, can also been regarded as charge carriers in battery chemistry.[2] Compared with metallic ions, nonmetallic charge carriers generally show remarkable advantages on dendrite-free behavior and intrinsic safety, excellent low-temperature performance, and fast rate-capability. Especially, ammonium ion delivers some unique properties as charge carriers on the lightest molar mass of 18 $g\,mol^{-1}$ and has the smallest hydrated ionic size to facilitate fast diffusion in aqueous electrolytes.[3] Compared with proton and hydronium, NH_4^+ is less corrosive and suffers less hydrogen evolution.[4] Taking in account of these merits, recently ammonium-ion aqueous battery has attracted tremendous interests as next-generation batteries. Typically, Ji et al. first reported "rocking-chair" NH_4^+ battery of the full-cell configuration by employing an ammonium Prussian white analogue, $(NH_4)_{1.47}Ni[Fe(CN)_6]_{0.88}$, as the cathode, perylenetetracarboxylic diimide (PTCDI), as the anode in aqueous $(NH_4)_2SO_4$ electrolyte in 2017.[5] Note that Prussian white analogues display a stable discharge plateau at 0.83 V, its discharge capacity less than 60 $mAh\,g^{-1}$ drastically limits the battery energy density. Most recently, much enhanced capacity for NH_4^+ storage has been found in some inorganic oxides, including layered V_2O_5,[6] hexagonal MoO_3,[7] WO_3,[8] MnO_x.[9] Nevertheless, one challenge of these inorganic compounds is the absence of a stable potential plateau with a rapidly descending potential output, suggesting that the electrochemical process is dominated by a surface redox pseudocapacitive mechanism rather than a desired battery-typed behavior. Accordingly, it is highly desired that once the stable potential output can be realized in inorganic compounds.

Layered phosphate compounds have attracted considerable research interests on energy storage owing to their unique layered structure with "inductive effect" originated from the strong P–O covalent bonds inside its in-plane structure remarkably enhances the iconicity of the V–O bonds.[10] Especially, layered hydrated vanadyl phosphate, $VOPO_4{\cdot}nH_2O$, is a bilayer structure where the adjacent layers are held together by weak bonding interactions with the characteristic of corner-shared [VO_6] octahedra linking to [PO_4] tetrahedra as a host layer,[11] and it has been already developed as a promising cathode material for pseudocapacitors,[12] Li^+,[13] Na^+,[14] Mg^{2+},[15] and Fe^{2+} [16] secondary batteries. Our previous study also demonstrates it can be used as robust anode in aqueous zinc-ion battery.[17]

However, for aqueous NH_4^+ storage, such a work is still in major challenging due to the poor structural stability of its layered framework. Previous study by other groups inferred that NH^{4+} ion storage in layered $VOPO_4{\cdot}2H_2O$ is

[*] Dr. F. Ye,[+] R. Pang,[+] C. Lu, Q. Liu, Prof. L. Hu
School of Materials Science and Engineering, Southeast University
Nanjing, 211189 (China)
E-mail: linfenghu@seu.edu.cn
Prof. Y. Wu
School of Energy and Environment, Southeast University
Nanjing, 211189 (P. R. China)
Dr. R. Ma
Research Center for Materials Nanoarchitectonics (MANA), National Institute for Materials Science (NIMS)
Namiki 1–1, Tsukuba, Ibaraki 305-0044 (Japan)
[+] These authors contributed equally to this work.

[**] A previous version of this manuscript has been deposited on a preprint server (https://doi.org/10.21203/rs.3.rs-2054819/v1).

impossible due to the removal of NH_4^+ from NH_4VOPO_4 leads to a phase change inevitably.[11b] Herein, we update this cognition and found highly reversible intercalation/de-intercalation behavior of NH_4^+ in layered $VOPO_4{\cdot}2H_2O$ host. Very stable discharge potential plateau at 0.4 V based on reference electrode has been observed with a high discharge capacity of 154.6 mAh g^{-1} at 0.1 A g^{-1}, which is more appealing compared with all inorganic and organic compounds reported recently. A rocking-chair ammonium-ion full cell with the $VOPO_4{\cdot}2H_2O$//NH_4OTf//PTCDI configuration exhibited a specific capacity of 55 mAh g^{-1}, an average operating voltage of about 1.0 V and excellent long-term cycling stability over 500 cycles with a coulombic efficiency of 99 %.

Results and Discussion

Powder sample of layered, hydrated vanadyl phosphate was synthesized via a conventional refluxing method reported previously.[12] X-ray diffraction (XRD) pattern in Figure 1a demonstrates a highly pure product which can be indexed to $VOPO_4{\cdot}nH_2O$ (JCPDS 84-0111, S.G. *P4/nmm*).[15] The very sharp (001) diffraction peak corresponds to a basal spacing of 7.4 Å, suggesting the high crystallinity with preferred [00*l*] (*l* = 1, 2) orientation. Thermogravimetric analysis (TGA) result depicts a weight loss of 17.3 % at 50–150 °C of the sample, which indicates the existence of two crystal water in per crystal ($VOPO_4{\cdot}2H_2O$, Figure S1). Fourier transform infrared (FTIR) spectrum in Figure 1b is well consistent with the previously reported result with the presence of lattice water in the structure.[17a] The characteristic peaks located at 1138, 951, 672, and 556 cm^{-1} can be assigned to the υ(P–O), υ(V–O), δ(V–P–O), and δ(O–P–O) vibrational modes in the $VOPO_4$ host, respectively. Furthermore, the peak at 3300 cm^{-1} and the hump around 1620 cm^{-1} corresponds to the interlayer lattice water, and another one at 3580 cm^{-1} are assigned to the bending mode of water (υ_{HOH}). Scanning electron microscope (SEM) observation indicates the as-synthesized $VOPO_4{\cdot}2H_2O$ comprises two-dimensional nanosheets with well-defined rectangular shape (Figure 1d and e). The later size of the rectangular nanosheet can be estimated as 10 μm × 16 μm. Transmission electron microscope (TEM) image also confirms the semitransparent nanosheet morphology with regular rectangular shape (Figure 1f). The in-plane selected area electron diffraction (SAED) pattern along the c axis taken from an individual nanosheet exhibited sharp cubic diffraction spots, verifying its single-crystal nature. The corresponding energy dispersive spectrum (EDS)-mapping further confirms uniform distribution of O, P, V elements in the nanosheet (Figure 1h). All of the aforementioned characterizations demonstrate that high-quality $VOPO_4{\cdot}2H_2O$ sample has been successfully obtained.

To investigate the ammonium-ion storage behavior of the $VOPO_4{\cdot}2H_2O$ cathode, Swagelok-type cells with a three-electrode configuration were assembled with $VOPO_4{\cdot}2H_2O$@carbon paper cathode, activated carbon (AC) counter electrode and an Ag/AgCl reference electrode. The $VOPO_4{\cdot}2H_2O$ cathode delivered capacities of 154.6, 119.2, 102.2, 85.1 mAh g^{-1} at the current rates of 0.1, 0.2, 0.5, 1.0 A g^{-1} in the 2.0 M NH_4OTf aqueous electrolyte (Figure 2a). The charge storage kinetics at the marked peaks are analyzed according to the peak current (i) dependence on and scan rate (v) as $i = av^b$.[18] The corresponding b values are calculated as 0.73, 0.75, 0.66, respectively, indicating that the kinetic behavior is controlled by both ion diffusion process and pseudocapacitance effect (Figure S2). Electro-

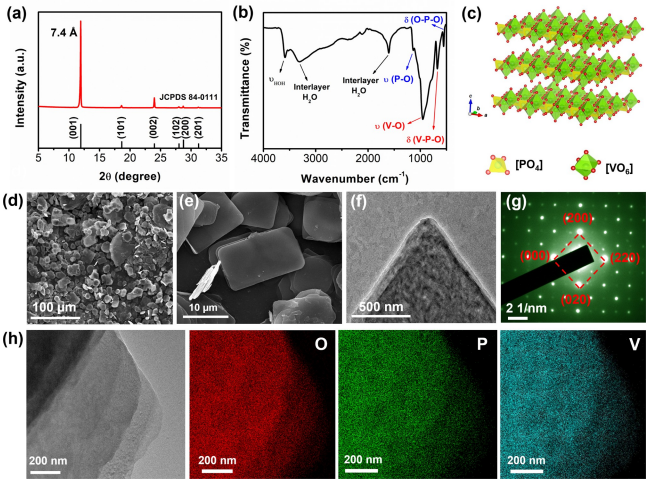

Figure 1. a) XRD pattern; b) FTIR spectra; c) crystal structure; d), e) Typical SEM image; f) TEM image and g) the corresponding SAED pattern of $VOPO_4{\cdot}2H_2O$ sample. h) EDS-mapping result of O, P, V elements in the $VOPO_4{\cdot}2H_2O$ nanosheet.

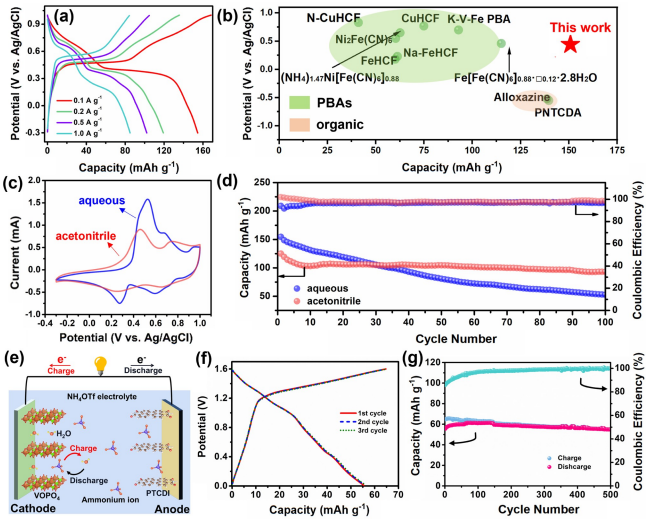

Figure 2. a) GCD profiles at various current rates of 0.1, 0.2, 0.5, 1.0 A g^{-1} in NH_4OTf aqueous electrolyte. b) Comparison of $VOPO_4{\cdot}2H_2O$ cathode to previously typical PBAs and organic cathodes on discharge potential plateau versus specific capacity. c) CV curves in NH_4OTf aqueous and anhydrous acetonitrile electrolyte, respectively. d) Long-term cycle test in aqueous NH_4OTf electrolyte and anhydrous acetonitrile electrolyte, respectively. e) Schematic structure of the $VOPO_4{\cdot}2H_2O$//PTCDI full cell. f) GCD curves at 0.1 A g^{-1}. g) Cycle performance at 0.1 A g^{-1}.

chemical impedance spectroscopy (EIS) spectra of our $VOPO_4{\cdot}2H_2O$ cathode (Figure S3) delivered two semicircles in the high-frequency area and a line in the low-frequency area, which corresponding to the ion diffusion resistance of 3.6 Ω in the interlayer of $VOPO_4{\cdot}2H_2O$ cathode, a charge transfer resistance of 9.1 Ω, and a Warburg diffusion impendence of 14.5 Ω, respectively. It should be noteworthy that a very stable discharge plateau at 0.40 V has been observed in our $VOPO_4{\cdot}2H_2O$ cathode, which is quite different with the one recently reported in inorganic oxide-based cathodes for ammonium-ion storage.[6–9] Besides, such a stable discharge plateau could be also observed in other common electrolyte salt solutions (e.g., $(NH_4)_2SO_4$, NH_4Cl, NH_4Ac, etc., Figure S4). Undoubtedly, the appearance of this stable discharge plateaus is very desirable and promising to construct full NH_4^+ battery toward practical applications. On the other hand, compared with the previously developed cathodes (metal-organic PBAs and some organic compounds) with stable discharge plateau, our $VOPO_4{\cdot}2H_2O$ cathode delivers superior specific capacity as shown in Figure 2b.[19] The combination of ultrastable charge/discharge potential plateau and high specific capacity makes this material a potential candidate for ammonium-ion storage cathode, which is more appealing compared with the various conventional cathode materials including both inorganic and organic compounds.

It is known that H^+ insertion/extraction is generally observed in aqueous batteries.[20] To identify whether this H^+ insertion/extraction process occurs or not in our system, we compared the electrochemical performance in NH_4OTf using aqueous electrolyte and nonaqueous acetonitrile electrolyte, respectively. Higher specific capacity was observed in aqueous electrolyte than that in acetonitrile (Figure S5). As shown in the CV curve (Figure 2c), two pairs of redox peaks located at 0.7/0.75 V and 0.4/0.62 V has been detected in aqueous electrolyte, respectively. Note that the similar shape of the CV profile was observed in the case of anhydrous acetonitrile solvent with two pair of redox peaks located at 0.75/0.8 V and 0.4/0.58 V, which ruling out the possible contribution from H^+ insertion/extraction in our layered $VOPO_4{\cdot}2H_2O$ host. The cycling performance of $VOPO_4{\cdot}2H_2O$ cathode was further studied at a current density of $0.1\ A\,g^{-1}$ (Figure 2d). Apparently, the $VOPO_4{\cdot}2H_2O$ cathode exhibits superior cycling performance in anhydrous acetonitrile to that in aqueous electrolyte. The former delivered very stable lifespan over 100 cycles with a 74.3 % capacity retention of the initial capacity of $125.1\ mAh\,g^{-1}$ and a coulombic efficiency close to 100 %. However, the latter exhibits apparent capacity decay with inferior capacity of $52.6\ mAh\,g^{-1}$ after 100 cycles (capacity retention: 34.1 %). The inferior cycling stability in aqueous electrolyte should be attributed to the decomposition/dissolution of $VOPO_4{\cdot}2H_2O$.[21] In brief, $VOPO_4{\cdot}2H_2O$ generally transforms into VO_x with the release of phosphate group into aqueous electrolyte, resulting in the capacity fading during the discharging/charging cycling.

On the basis of the above results, we further attempted to construct a rocking-chair NH_4-ion battery using our $VOPO_4{\cdot}2H_2O$ cathode. Figure 2e illustrates the schematic configuration of the battery, using commercial PTCDI with suitable reduction potential (see Figure S6) as the anode material and NH_4OTf acetonitrile solution as electrolyte. Figure S7 shows the typical CV curve of this $VOPO_4{\cdot}2H_2O$// NH_4OTf//PTCDI full cell at a scan rate of $0.2\ mV\,s^{-1}$. Clearly, the CV loop exhibits two widely spread cathodic peaks at 1.1 V and 0.7 V and a broad anodic peak at 1.2 V, respectively, which is in good agreement with the GCD profiles of the as-constructed battery after the initial activation process (Figure 2f). The specific capacity is $55\ mAh\,g^{-1}$, with an average operating voltage of about 1.0 V. Such a NH_4-ion full cell also demonstrates good long-term cycling stability over 500 cycles at the rate of $0.1\ A\,g^{-1}$ with a satisfactory capacity retention of $54.8\ mAh\,g^{-1}$ and the coulombic efficiency of approximately 99 % (Figure 2g).

We then studied the phase and morphology evolution of our $VOPO_4{\cdot}2H_2O$ nanosheets at different depths of long-term cycling. Ex situ XRD patterns of the pristine cathode and the one after 2, 10 to 50th cycles indicate no remarkable changes on phase structure. All of the peaks can be classified to the characteristic (00l) ($l=1, 2$) peaks of layered $VOPO_4{\cdot}2H_2O$ and carbon paper collector (labelled as star in Figure S8). The gradual decrease on the diffraction intensity of (001) peak suggests the degradation on crystallinity in a long-term cycling. SEM characterization of the cathode after 20 and 100 cycles indicates that the initial 2D ultrathin morphology can be well retained (Figure S9a, b). The corresponding TEM observation further demonstrates the maintaining of well-defined 2D nanosheet morphology with a smooth surface (Figure S10a, b). The corresponding SAED pattern (Figure S10c) taken from an individual nanosheet after 100 cycles shows squared arranged spots analogous to that of the pristine sample, demonstrating the single-crystal structure can be maintained during the charge/discharge process. However, it is difficult to record HRTEM image with clear lattice fringes due to the fact that the crystalline nanosheets were very easily destroyed under a short-time e-beam irradiation. More intuitively, the corresponding EDS-mapping results in Figure S10d further confirm the uniform dispersion of V, O, P in the nanosheets after 100 cycles lifespan. One can see the apparent existence of the N element the nanosheet with a uniform distribution from the N EDS-mapping. This result provides the evidence that NH_4^+ ions are indeed inserted into our layered $VOPO_4{\cdot}2H_2O$ framework.

We then performed various ex situ characterizations to unveil its underlying energy storage mechanism. To trace the structural evolution of $VOPO_4{\cdot}2H_2O$ electrode, ex situ XRD patterns (Figure 3b) were recorded at different charge/discharge states in the second cycle in aqueous system (A to K points in Figure 3a). As shown in Figure 3c, the initial position of the (001) peak was located at 12.2° with a d-spacing of 7.2 Å, and shifted slightly to a high angle when discharged into 0.7 V (state B), indicating the decrease in the d-spacing into 7.1 Å caused by NH_4^+ intercalation during the discharge process. Interestingly, further discharged this cathode to 0.4 V (state C), the (001) peak splits into two basal spacings of 6.8 Å and 6.5 Å, respectively. The appearance of two basal spacings in layered electrode during

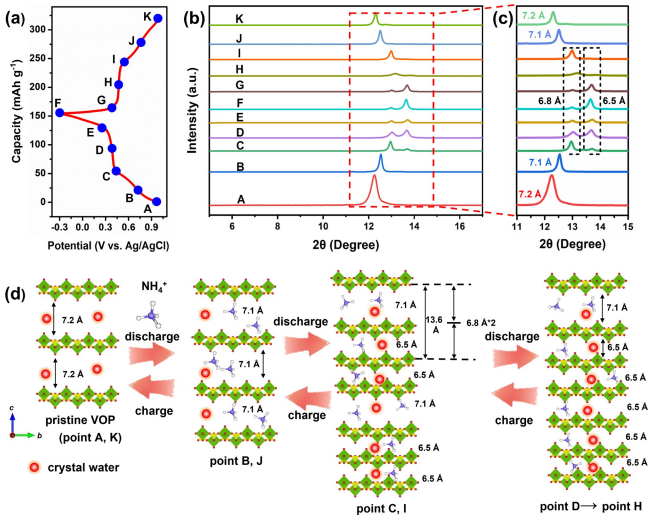

Figure 3. a)–c) XRD patterns at different potentials in the second GCD cycle. d) Schematic illustration of the interlayer d-spacing evolution of the layered $VOPO_4{\cdot}2H_2O$ during the charge/discharge process.

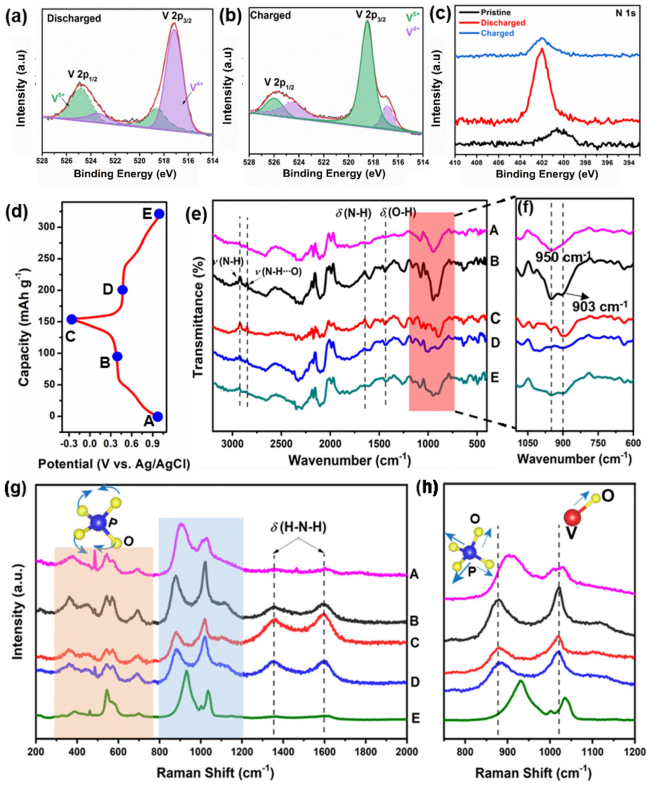

Figure 4. High-resolution V 2p XPS spectra at fully a) discharged and b) charged states. c) N 1s XPS spectra at different states. d)–f) FTIR and g), h) Raman spectra during one charge/discharge cycle.

the electrochemical process has been rarely observed, which should be attributed to the alternated stacking phenomenon on the topochemical transformation from Brucite into layered double hydroxides.[22] We notice that the summation of the 6.5 Å and 7.1 Å spacing is 13.6 Å, which is the twice of 6.8 Å just right. Such a coincidence inspires us to consider the co-existence of two different interlayer spacings of 6.5 Å and 7.1 Å spacing from C to F states. The disappearance of the 7.1 Å spacing implies any 7.1 Å spaced slab always adjacent with several 6.5 Å spaced slabs (as schematically illustrated in Figure 3d). In the other words, there is no consecutive stacking of 7.1 Å spaced slabs.[22] The diffraction intensity of the 6.8 Å basal spacing gradually decreased with the simultaneously increased intensity of the 6.5 Å spacing, suggesting the decrease on the amount of 7.1 Å spaced slab in the layered framework with the deep intercalation of NH_4^+. Upon charging from state F to K, the peak intensity ratio of 6.8 Å/6.5 Å peak exhibits a contrary tendency compared with the discharging process. Satisfactorily, this basal spacing well recovered to the initial position of 7.2 Å at the end of charging (K point), demonstrating the excellent structural reversibility with the well keep of high crystallinity during the NH_4^+ ion intercalation/de-intercalation process. Based on this ex situ XRD measurement, it is rational that the as-observed stable charge/discharge plateau is originated from the intercalation/de-intercalation of NH_4^+ ion in the open two-dimensional channel of the $VOPO_4{\cdot}2H_2O$ framework.

Ex situ XPS analysis was conducted to unveil the valence state evolution during the ammoniation/de-ammoniation process. Figure S11 depicts that the initial V valence state in the $VOPO_4{\cdot}2H_2O$ cathode is +5. Subsequently, at the fully discharged state at −0.3 V, the decrease on V valence state is evident by the co-existence of V^{4+} and V^{5+} in Figure 4a. Note that V^{4+} is dominated in the cathode, implying that the redox reaction at the transition metal V site in $VOPO_4{\cdot}2H_2O$ is responsible for the electrochemical charge storage. Upon fully charging to 1.0 V, the ultimate peak characteristic of V^{5+} is almost the same to that of the pristine cathode (Figure 4b), demonstrating the excellent reversibility of V valence evolution during the charge/discharge process. In addition, the high-resolution XPS of N 1s corresponded to the pristine, fully discharged and charged state of the $VOPO_4{\cdot}2H_2O$ cathode are demonstrated in Figure 4c. The intensity at fully discharged state is much higher than that of the pristine and fully charged electrodes, further supporting the NH_4^+ ion intercalation in the layered framework during the discharging process. FTIR spectra provide more insights on bonding chemistry during the NH_4^+ ion intercalation/de-intercalation. Figure 4d depicts the GCD profile in which five statuses are selected for ex situ FTIR study. After NH_4^+ intercalation (B and C), the stretching vibration of N–H bond gradually appear two peaks at 2922 and 2850 cm^{-1} (Figure 4e). The former is attributed to the stretching of N–H bonded to the $VOPO_4{\cdot}2H_2O$ host, while the latter (2850 cm^{-1}) is originated from the stretching of non-bonded N-H.[23] These two characteristic peaks can also be detected at the charge process (D and E) with de-intercalation of NH_4^+, suggesting some NH_4^+ ion residue in the $VOPO_4{\cdot}2H_2O$ framework in our cathode upon charging. This result is consistent with the aforementioned N 1s XPS spectra. In addition, the cathode sample displays a signal at ≈1647 cm^{-1} for the H-bonded N–H at B and C states, indicating the possible formation of

hydrogen bonds between the intercalated NH_4^+ and the $VOPO_4{\cdot}2H_2O$ host. This characteristic peak gradually disappears after charging at D and E states, which should be ascribed to the hydrogen bond formation/breaking accompanied with the NH_4^+ intercalation/de-intercalation in layered $VOPO_4{\cdot}2H_2O$. Similar phenomenon has also been found in other NH_4^+ storage materials including layered V_2O_5,[6] hexagonal MoO_3,[7] and MnO_x.[9] It is noteworthy that the peak intensity of V=O bond ($\approx$950 cm^{-1}) stretch decreased during the discharging process with a new peak at 903 cm^{-1} emerging as shown in the enlarged spectra (Figure 4f). In discharged states (B and C), the peak around $\approx$950 cm^{-1} gradually recovered to its initial intensity with a decrease on the density of the peak at 903 cm^{-1}. According to the previous report, the splitting of V=O bond stretches into red-shifted sub-peaks located at 923 cm^{-1} has been also found in bi-layered V_2O_5 as robust anode for ultrafast NH_4^+ storage due to the V=O are bound with NH_4^+.[24] In our case, it may also originate from the same chemical bonding between NH_4^+ during the intercalation process.

Subsequently, Raman characterization was complemented with the FTIR spectra to further identify the chemical bonding information. As shown in Figure 4g, two new Raman peaks located at 1390 and 1600 cm^{-1} respectively emerged at stage B and C during the discharge, which is ascribed to stretching vibration of N–H bond.[8] This result is well agreement with above-mentioned FTIR result. The maximal intensity appears in fully discharged C state, implying a continuous NH_4^+ intercalation process during the whole discharge stage. Upon charging, the ex situ Raman spectra shows a reduction in the N–H bond signal, and it is hardly distinguished at the fully charged state E, indicating the excellent structural reversibility of our $VOPO_4{\cdot}2H_2O$. Meanwhile, the peak located at around 1030 cm^{-1} is generated from the stretching mode of V=O in $[VO_6]$ octahedron from the $VOPO_4{\cdot}2H_2O$ host.[25] Due to the hydrogen bond formation between the NH_4^+ and $VOPO_4$ layer (V=O···H) and the resultant valence reduction of V from V^{5+} to V^{4+}, a slight red shift is thus detected for this featured peak with NH_4^+ intercalation during the discharge process (B, C). Upon fully charging accompanied with the de-ammonization, this V=O signal can well recover to the initial position. Furthermore, the same tendency of red shift was also observed on the stretching vibration peak of P–O bond located at around 940 cm^{-1}. Since the hydrogen bond between the interlayered H_2O molecule and $VOPO_4$ layer (P–O···H–O) is partially displaced by NH_4^+ incorporation (P–O···H–N), intensity of such the hydrogen bonding is therefore depressed, leading to mitigation of the steric hindrance of the P–O stretching mode with lower energy (Figure 4h).[12] Additionally, for the bending vibration peak of P–O bond between 500–600 cm^{-1}, a noteworthy peak splitting occurs during the NH_4^+ ion intercalation and is mitigated after NH_4^+ ion de-intercalation. This phenomenon might be ascribed to the possible lattice deformation upon the NH_4^+ de-intercalation in the layered framework.[12,26]

We have confirmed that NH_4^+ ions are indeed inserted into the interlayer of the $VOPO_4{\cdot}2H_2O$ host during the electrochemical process. Density functional theory (DFT) calculations further provide theoretical insights on the insertion/extraction process of NH_4^+. We built a calculation configuration of the conjecture based on the substitution of crystal water by NH_4^+ cation. After a full relaxation, the distribution morphology of H_2O molecules in the interlayer space of $VOPO_4$ bilayers (Figure 5a) suggests two possible active sites for the intercalated ammonium ions absorption: P top (above the center of $[PO_4]$) and V top (above the center of $[VO_6]$), respectively. Thereafter, the substitution process is simulated in a $2\times2\times1$ supercell with the formula of $(VOPO_4)_2{\cdot}4H_2O$, in which the ammonium ions are introduced one by one (all atomic schemes are shown in Figure S12), and the relationship between total energy (E_{total}) and interlayer distance d of each composition of $(NH_4)_xVOPO_4{\cdot}(2-x)H_2O$ ($x=0$, 0.5, 1, …) has been established as given in Figure 5b. While the structure achieves its minimum total energy, the simulation results indicate that the optimal interlayer distance of $VOPO_4{\cdot}2H_2O$ without any NH_4^+ ion intercalation is theoretically 7.7 Å, close to the value of 7.2 Å in our experiments. With one substitution, the resultant $(NH_4)_{0.5}VOPO_4{\cdot}1.5H_2O$ possessing an ammonium ion at P top (blue line) exhibits an absolutely lower total energy than that at V top (green line). Correspondingly, the optimal interlayer distance of $(NH_4)_{0.5}VOPO_4{\cdot}1.5H_2O$ is determined to be 7.3 Å, and the substitution formation energy is calculated to be −3.38 eV, the negative value of which implies the feasibility and spontaneity of the substitution behavior. Similar conclusion could be obtained in $(NH_4)VOPO_4{\cdot}H_2O$ with further NH_4^+ substitution, that with two NH_4^+ cations occupying P–P top (blue line) is energetically more favorable than P–V top (purple line) and V–V

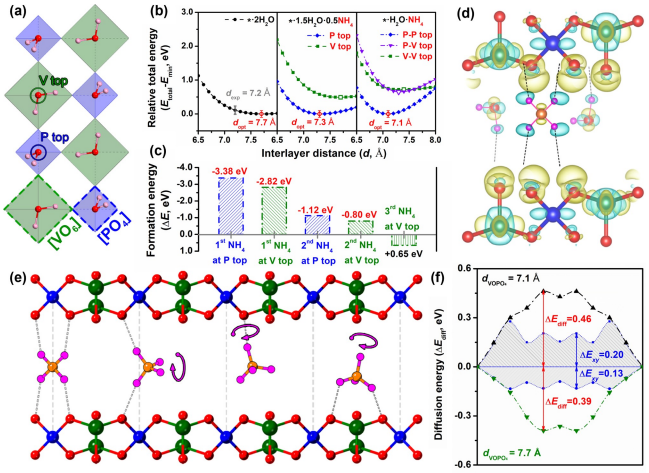

Figure 5. a) Atomic scheme of $VOPO_4{\cdot}2H_2O$ showing the distribution of H_2O molecules at P top (center of $[PO_4]$) and V top (center of $[VO_6]$); b) the relationship between total energy (E_{total}) and interlayer distance of $(NH_4)_xVOPO_4{\cdot}(2-x)H_2O$ ($x=0$, 0.5, 1, ...); c) the calculated substitution formation energy (ΔE) of NH_4^+ ion for H_2O; d) the computed difference charge density of $(NH_4)VOPO_4{\cdot}H_2O$ showing hydrogen bonds (in dash lines); e) diffusion scheme of NH_4^+ ion in the interlayer space of $VOPO_4$ bilayers (surrounding H_2O are not shown in the figure); f) the diffusion energies (ΔE_{diff}) calculated at the interlayer distances of 7.1 Å (top) and 7.7 Å (bottom), respectively, with shaded area showing the in-plane barrier contribution (ΔE_{xy}).

top (green line) configurations. In this case, the optimal interlayer distance further decreases to 7.1 Å together with a negative but reduced formation energy of −1.12 eV. However, further substituting crystal water at V top site gives rise to a positive formation energy of 0.65 eV, as shown in Figure 5c, implying that just a half of the indigenous crystal water in $VOPO_4{\cdot}2H_2O$ can be replaced during the discharge process, leading to the ultimately formation of $(NH_4)VOPO_4{\cdot}H_2O$, in which the NH_4^+ intercalations are distributing at P top site. It is noteworthy that a theoretical interlayer distance evolution from 7.7 Å to 7.1 Å during the substitution process is in well consistent with the aforementioned ex situ XRD characterization (Figure 3), further identifying the validity of our proposed configuration with the substitution of H_2O by NH_4^+ cation in layered framework. When it comes to the charge stage, during which process the vanadium element of [VO_6] donates its electrons showing a valence state rising from V^{4+} to V^{5+} as claimed in our XPS characterization, the deintercalation of NH_4^+ cation from the interlayer distance of $VOPO_4$ bilayers would occur due to the electrostatic repulsion effect. Thereafter, the H_2O molecules are capable of re-occupying the vacant sites from the deintercalated NH_4^+ cations with a negative formation energy of −1.11 eV. As a result, the contraction (from 7.7 Å to 7.1 Å) and expansion (from 7.1 Å to 7.7 Å) of the interlayer distance of $VOPO_4$ during the discharge ($VOPO_4{\cdot}2H_2O \rightarrow (NH_4)VOPO_4{\cdot}H_2O$) and charge ($(NH_4)VOPO_4{\cdot}H_2O \rightarrow VOPO_4{\cdot}2H_2O$) stages are invertible, which is experimentally proved in the ex situ XRD characterization. The difference charge density mapped in Figure 5d demonstrates that the formation of hydrogen bonds plays a significant role in narrowing the interlayer distance of $VOPO_4$ with NH_4^+ intercalation: an obvious electron exchange between H of [NH_4^+] (blue, gains electrons) and O of [PO_4] (yellow, donates electrons) can be observed, with a representative bonding length of 3.09 Å (N–H···O). Moreover, the bonding features of [VO_6] octahedron are found to get strongly affected by the intercalated NH_4^+ ion, which can be also found in the electronic property analysis (Figure S13). Figure 5e shows the diffusion behavior of the NH_4^+ ion in the interlayer space of $VOPO_4$ bilayer between two adjacent P top sites. Previous studies have revealed the transport mechanism of NH_4^+ remarkably differs from that of metal ions. Metal ions (Li^+, Na^+, K^+, Zn^{2+}, et al.) generally have spherical shape with no preferred orientations. While in our case, however, the ammonium ion shows a tetrahedral-shaped multipole, which has to twist and rotate to maintain a subset of coordinated H-bonds with adjacent oxygen atoms from the crystal host, just like a monkey swinging mechanism.[4] Accordingly, the diffusion energies of the NH_4^+ ion along the "P top - P top" path are calculated with the results depicted in Figure 5f. It can be seen that the contraction of interlayer distance from 7.7 Å (initial) to 7.1 Å (final) poses limited impacts on rising the diffusion barrier, with the values of E_{diff} increased from 0.39 eV (grey line) to 0.46 eV (black line). By distinguishing the energy barrier contributions from xy plane (shaded area) and z axis (blank area), it is revealed that the main resistance is related with the interaction by in-plane H_2O molecules, accounting for more than 50 % of the total energy barrier around the transition state (TS) positions. The low diffusion energy barrier ranging from 0.39 eV to 0.46 eV endows the outstanding theoretical repeatability of our $VOPO_4$ host.

The above calculation results have revealed the crystal water molecules in the interlayer of $VOPO_4$ play critical roles in the NH_4^+ insertion. To further confirm this crystal water enhancement effect, we carried out the annealing treatment of $VOPO_4{\cdot}2H_2O$ precursor at 100 °C (denoted as VOP-100) and 400 °C (VOP-400) in air to prepare the dehydrated samples with different water contents. The corresponding XRD patterns of both VOP-100 and VOP-400 in Figure 6a indicate that the initial (001) peak of $VOPO_4{\cdot}2H_2O$ greatly decreased in diffraction intensity, and slightly shifted to a higher degree as shown in the enlarged pattern (Figure 6b). Meanwhile, a new (001) peak appears at about 21.4° originated from the non-crystal water phase ($VOPO_4$, JCPDS: 27-0947). This result identifies that both VOP-100 and VOP-400 samples are a mixture of $VOPO_4{\cdot}2H_2O$ and $VOPO_4$ phase. Further confirmed by the TGA characterization, the VOP-100 and VOP-400 sample contains 0.47 and 0.19 crystal water respectively (Figure 6c). As shown in Figure 6d, the FTIR spectra of VOP-100 and VOP-400 samples deliver the similar characteristic peaks as that of hydrated $VOPO_4{\cdot}2H_2O$ in the wavenumber range of 500–1500 cm^{-1}, demonstrating that the crystal structure of $VOPO_4$ still remain intact after losing the lattice water molecules. SEM observation suggests the loss of regular shape and smooth surface after annealing (Figure 6e, f). Subsequently, GCD profiles of initial $VOPO_4{\cdot}2H_2O$, VOP-100 and VOP-400 samples were recorded in Swagelok-type cell using nonaqueous 2.0 M acetonitrile NH_4OTf electrolyte. As shown in Figure 6g, the discharge plateau gradually disappeared with the decrease of crystal water contents in the sample, and the annealed VOP-100 and VOP-400 samples respectively exhibit a much lower specific capacity of 88.8 and 59.4 mAh g^{-1} compared with that of hydrated

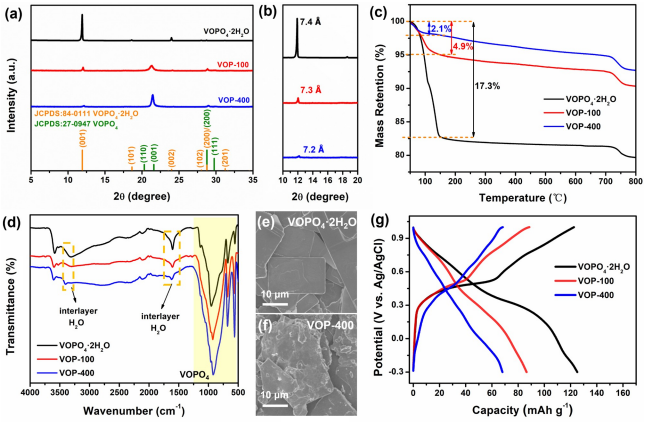

Figure 6. a) XRD patterns and b) enlarged pattern of $VOPO_4{\cdot}2H_2O$, VOP-100 and VOP-400. c) Corresponding TGA curves and d) FTIR spectra. e), f) SEM images of $VOPO_4{\cdot}2H_2O$ and VOP-400. g) GCD curves of $VOPO_4{\cdot}2H_2O$, VOP-100 and VOP-400 cathodes in NH_4OTf acetonitrile electrolyte at 0.1 A g^{-1}.

$VOPO_4{\cdot}2H_2O$ (122.8 mAh g^{-1}). The cycling performance of the de-hydrated samples were further evaluated at a current density of 0.1 A g^{-1} (Figure S14), which is also remarkably inferior to the hydrated sample before annealing (only 51.4 mAh g^{-1} and 38.5 mAh g^{-1} after 40 cycles for VOP-100 and VOP-400, respectively). In addition, the similar phenomenon on performance degeneration was observed in aqueous electrolyte (2.0 M NH_4OTf aqueous electrolyte in Figure S15 and S16). All of these results reveal that the crystal water molecules in the interlayer of $VOPO_4$ play an important role in NH_4^+ ion storage, which has also been reported in layered manganese oxide cathode for aqueous zinc ion battery by Choi et al.[27]

Conclusion

In conclusion, we demonstrated layered hydrated vanadyl phosphate ($VOPO_4{\cdot}2H_2O$) can be a suitable NH_4^+ ion storage host with a specific capacity of 154.6 mAh g^{-1} and an average potential of 0.4 V (vs. Ag/AgCl). The simultaneous appearance on both high capacity and stable working potential makes this material a very appealing candidate for NH_4^+ ion battery application. The stable discharge potential plateau comes from the reversible intercalation/de-intercalation of NH_4^+ in the interlayer spacing followed by an alternated stacking mechanism. We reveal that the crystal water in the $VOPO_4{\cdot}2H_2O$ host plays a key role in the structural stability and promotes the NH_4^+ ion storage behavior. Theoretical DFT calculations suggest a unique crystal water substitution process by ammonium ion during the intercalation process accompanied with the formation/breaking of hydrogen bonds. Our results provide new insight into the intercalation/de-intercalation of NH_4^+ ions in layered hydrated phosphate with unique alternated stacking configuration and crystal water promoting effect.

Acknowledgements

This work was financially supported by the Natural Science Foundation of Jiangsu Province (Grants No. BK20211516), the National Natural Science Foundation of China (Nos. 52171203, 51872051), the National Key Research and Development Program of China (Grant No. 2021YFB2400400), the State Key Laboratory of New Ceramic and Fine Processing of Tsinghua University (No. KF202102) and the Fundamental Research Funds for the Central Universities (2242023K5001).

Conflict of Interest

The authors declare no conflict of interest.

Data Availability Statement

The data that support the findings of this study are available from the corresponding author upon reasonable request.

Keywords: Aqueous Ammonium-Ion Batteries · Discharge Plateau · Intercalation/De-Intercalation · Layered Framework · $VOPO_4{\cdot}2H_2O$

[1] a) C. L. Zhao, Q. D. Wang, Z. P. Yao, J. L. Wang, B. S. Lengeling, F. X. Ding, X. G. Qi, Y. X. Lu, X. D. Bai, B. H. Li, H. Li, A. A. Guzik, X. J. Huang, C. Delmas, M. Wagemaker, L. Q. Chen, Y. S. Hu, *Science* **2020**, *370*, 708; b) Q. F. Zhang, X. L. Cheng, C. X. Wang, A. M. Rao, B. G. Lu, *Energy Environ. Sci.* **2021**, *14*, 965; c) D. Kundu, B. D. Adams, V. Duffort, S. H. Vajargah, L. F. Nazar, *Nat. Energy* **2016**, *1*, 16119; d) H. Dong, O. Tutusaus, Y. L. Liang, Y. Zhang, Z. Lebens-Higgins, W. L. Yang, R. Mohtadi, Y. Yao, *Nat. Energy* **2020**, *5*, 1043; e) M. C. Lin, M. Gong, B. G. Lu, Y. P. Wu, D. Y. Wang, M. Y. Guan, M. Angell, C. X. Chen, J. Yang, B. J. Hwang, H. J. Dai, *Nature* **2015**, *520*, 325; f) X. L. Ji, *Energy Environ. Sci.* **2019**, *12*, 3203; g) A. Rahil, E. Partenie, M. Bowkett, M. H. Nazir, M. M. Hussain, *Battery Energy* **2022**, *1*, 20210001; h) J. L. Yang, X. Zhao, M. Y. Ma, Y. Liu, J. P. Zhang, X. L. Wu, *Carbon Neutralization* **2022**, *1*, 247.

[2] a) G. J. Liang, F. N. Mo, X. L. Ji, C. Y. Zhi, *Nat. Rev. Mater.* **2021**, *6*, 109; b) Z. W. Guo, J. H. Huang, X. L. Dong, Y. Y. Xia, L. Yan, Z. Wang, Y. G. Wang, *Nat. Commun.* **2020**, *11*, 959.

[3] a) J. Han, A. Varzi, S. Passerini, *Angew. Chem. Int. Ed.* **2022**, *61*, e202115046; b) R. D. Zhang, S. Wang, S. L. Chou, H. L. Jin, *Adv. Funct. Mater.* **2022**, *32*, 2112179.

[4] D. L. Chao, H. J. Fan, *Chem* **2019**, *5*, 1357.

[5] X. Y. Wu, Y. T. Qi, J. J. Hong, Z. F. Li, A. S. Hernandez, X. L. Ji, *Angew. Chem. Int. Ed.* **2017**, *56*, 13026.

[6] S. Y. Dong, W. Shin, H. Jiang, X. Y. Wu, Z. F. Li, J. Holoubek, W. F. Stickle, B. Key, C. Liu, J. Lu, P. A. Greaney, X. G. Zhang, X. L. Ji, *Chem* **2019**, *5*, 1537.

[7] G. J. Liang, Y. L. Wang, Z. D. Huang, F. N. Mo, X. L. Li, Q. Yang, D. H. Wang, H. F. Li, S. M. Chen, C. Y. Zhi, *Adv. Mater.* **2020**, *32*, 1907802.

[8] Y. Z. Zhang, J. Liang, Z. H. Huang, Q. Wang, G. Y. Zhu, S. Y. Dong, H. F. Liang, X. C. Dong, *Adv. Sci.* **2022**, *9*, 2105158.

[9] Y. Song, Q. Pan, H. Z. Lv, D. Yang, Z. M. Qin, M. Y. Zhang, X. Q. Sun, X. X. Liu, *Angew. Chem. Int. Ed.* **2021**, *60*, 5718.

[10] a) D. A. Kuznetsov, B. Han, Y. Yu, R. R. Rao, J. Hwang, Y. Roman-Leshkov, Y. Shao-Horn, *Joule* **2018**, *2*, 225; b) Y. Zhu, Y. M. Qian, Z. Y. Ju, Y. J. Ji, Y. Yan, Y. Y. Liu, G. H. Yu, *ACS Nano* **2020**, *14*, 13824.

[11] a) H. Y. Shi, Z. Q. Jia, W. L. Wu, X. Zhang, X. X. Liu, X. Q. Sun, *Chem. Eur. J.* **2020**, *26*, 8190; b) N. A. Chernova, M. F. V. Hidalgo, C. Kaplan, K. Lee, I. Buyuker, C. Siu, B. H. Wen, J. Ding, M. Zuba, K. M. Wiaderek, I. D. Seymour, S. Britto, L. F. J. Piper, S. P. Ong, K. W. Chapman, C. P. Grey, M. S. Whittingham, *Adv. Energy Mater.* **2020**, *10*, 202002638.

[12] C. Z. Wu, X. L. Lu, L. L. Peng, K. Xu, X. Peng, J. L. Huang, G. H. Yu, Y. Xie, *Nat. Commun.* **2013**, *4*, 2431.

[13] T. Nakato, Y. Furumi, N. Terao, T. Okuhara, *J. Mater. Chem.* **2000**, *10*, 737.

[14] G. He, W. H. Kan, A. Manthiram, *Chem. Mater.* **2016**, *28*, 682.

[15] X. Ji, J. Chen, F. Wang, W. Sun, Y. J. Ruan, L. Miao, J. J. Jiang, C. S. Wang, *Nano Lett.* **2018**, *18*, 6441.

[16] K. Xu, X. Y. Wu, S. K. Sandstrom, J. J. Hong, H. Jiang, X. Chen, X. L. Ji, *Adv. Mater.* **2021**, *33*, 2105234.

[17] a) F. Hu, Z. Y. Wu, C. J. Lu, F. Ye, Q. Liu, Z. M. Sun, *Energy Environ. Sci.* **2021**, *14*, 4095; b) Z. Y. Wu, C. J. Lu, F. Ye, L.

Zhang, L. Jiang, Q. Liu, H. L. Dong, Z. M. Sun, L. F. Hu, *Adv. Funct. Mater.* **2021**, *31*, 2106816.
[18] a) Y. Yan, B. Hao, D. Wang, G. Chen, E. Markweg, A. Albrecht, P. Schaaf, *J. Mater. Chem. A* **2013**, *1*, 14507; b) Y. Gogotsi, R. M. Penner, *ACS Nano* **2018**, *12*, 2081.
[19] a) Z. Z. Zhao, W. Zhang, M. Liu, D. Wang, X. Y. Wang, L. R. Zheng, X. Zou, Z. Z. Wang, D. B. Li, K. K. Huang, W. T. Zheng, *Energy Environ. Mater.* **2022**, *6*, e12342; b) X. Y. Wu, Y. K. Xu, H. Jiang, Z. X. Wei, J. J. Hong, A. S. Hernandez, F. Du, X. L. Ji, *ACS Appl. Energy Mater.* **2018**, *1*, 3077; c) C. Y. Li, D. X. Zhang, F. X. Ma, T. Y. Ma, J. Wang, Y. H. Chen, Y. S. Zhu, L. J. Fu, Y. P. Wu, W. Huang, *ChemSusChem* **2019**, *12*, 3732; d) X. K. Zhang, M. T. Xia, T. T. Liu, N. Peng, H. X. Yu, R. T. Zheng, L. Y. Zhang, M. Shui, J. Shu, *Chem. Eng. J.* **2021**, *421*, 127767; e) S. Qiu, Y. K. Xu, X. Li, S. K. Sandstrom, X. Y. Wu, X. L. Ji, *Electrochem. Commun.* **2021**, *122*, 106880; f) J. J. Xing, X. L. Fu, S. D. Guan, Y. Zhang, M. Lei, Z. J. Peng, *Appl. Surf. Sci.* **2021**, *543*, 148843; g) S. Y. Li, M. T. Xia, C. X. Xiao, X. K. Zhang, H. X. Yu, L. Y. Zhang, J. Shu, *Dalton Trans.* **2021**, *50*, 6520; h) X. K. Zhang, M. T. Xia, H. X. Yu, J. W. Zhang, Z. W. Yang, L. Y. Zhang, J. Shu, *Nano-Micro Lett.* **2021**, *13*, 139; i) Y. Ma, T. J. Sun, Q. S. Nian, S. B. Zheng, T. Ma, Q. R. Wang, H. H. Du, Z. L. Tao, *Nano Res.* **2022**, *15*, 2047; j) H. X. Yu, J. X. Xu, C. C. Deng, M. T. Xia, X. K. Zhang, J. Shu, Z. B. Wang, *ACS Appl. Energy Mater.* **2021**, *4*, 9594; k) H. X. Yu, L. Y. Fan, H. H. Yan, C. C. Deng, L. Yan, J. Shu, Z. B. Wang, *Inorg. Chem. Front.* **2022**, *9*, 2001.
[20] a) S. Wang, Z. S. Yuan, X. Zhang, S. S. Bi, Z. Zhou, J. L. Tian, Q. C. Zhang, Z. Q. Niu, *Angew. Chem. Int. Ed.* **2021**, *60*, 7056; b) X. Shi, X. Y. Liu, E. Z. Wang, X. S. Cao, Y. X. Yu, X. N. Cheng, X. H. Lu, *Carbon Neutralization* **2023**, *2*, 28; c) Y. X. Guo, Y. X. Zhang, H. B. Lu, *Battery Energy* **2022**, *1*, 20210014.
[21] H. Y. Shi, Y. Song, Z. M. Qin, C. C. Li, D. Guo, X. X. Liu, X. Q. Sun, *Angew. Chem. Int. Ed.* **2019**, *58*, 16057.
[22] R. Z. Ma, J. B. Liang, X. H. Liu, T. Sasaki, *J. Am. Chem. Soc.* **2012**, *134*, 19915.
[23] S. M. Bak, R. M. Qiao, W. L. Yang, S. Lee, X. Q. Yu, B. Anasori, H. Lee, Y. Gogotsi, X. Q. Yang, *Adv. Energy Mater.* **2017**, *7*, 1700959.
[24] a) T. Y. Zhai, H. M. Liu, H. Q. Li, X. S. Fang, M. Y. Liao, L. Li, H. S. Zhou, Y. Koide, Y. Bando, D. Golberg, *Adv. Mater.* **2010**, *22*, 2547; b) S. D. Perera, R. B. Archer, C. A. Damin, R. Mendoza-Cruz, C. P. Rhodes, *J. Power Sources* **2017**, *343*, 580.
[25] L. Beneš, K. Melánová, M. Trchová, P. Čapková, P. Matějka, *Eur. J. Inorg. Chem.* **1999**, 2289.
[26] Y. J. Fang, Q. Liu, L. F. Xiao, Y. C. Rong, Y. D. Liu, Z. X. Chen, X. P. Ai, Y. L. Cao, H. X. Yang, J. Xie, C. J. Sun, X. Y. Zhang, B. Aoun, X. R. Xing, X. H. Xiao, Y. Ren, *Chem* **2018**, *4*, 1167.
[27] K. W. Nam, H. Kim, J. H. Choi, J. W. Choi, *Energy Environ. Sci.* **2019**, *12*, 1999.

Manuscript received: March 8, 2023
Accepted manuscript online: April 11, 2023
Version of record online: May 4, 2023